

# Kinematics analysis and testing of novel 6-P-RR-R-RR parallel platform with offset RR-joints

Proc IMechE Part C:  
J Mechanical Engineering Science  
0(0) 1–19  
© IMechE 2018  
Article reuse guidelines:  
sagepub.com/journals-permissions  
DOI: 10.1177/0954406218817001  
journals.sagepub.com/home/pic



Ha-si-ao-qi-er Han<sup>1,2</sup> , Chun-Yang Han<sup>1,2</sup>, Zhen-Bang Xu<sup>1</sup>,  
Ming-Chao Zhu<sup>1</sup>, Yang Yu<sup>1</sup> and Qing-Wen Wu<sup>1</sup>

## Abstract

This paper presents a novel six-degree-of-freedom (6-DOF) parallel platform that is used as the third mirror adjustment system of a large space telescope. In order to meet the design requirements of high precision, a large load–size ratio, and high stiffness in both the transverse and the vertical directions, the parallel platform is designed to be a 6-P-RR-R-RR structure via use of offset RR-joints. The inverse kinematics problem of the designed platform with offset RR-joints is much more complicated than that of a parallel platform with common universal joints owing to the presence of joint-dependent variables in the former problem. In this study, inverse kinematics of the designed parallel platform is mathematically modeled and the Newton–Raphson numerical iterative computation is performed. The accuracy and effectiveness of the proposed mathematical approach are verified by numerical co-simulations using MATLAB and ADAMS. The initial position of the platform is determined by a precision measuring arm. A test system is constructed, and then inverse kinematics solution, resolutions and adjusting steps accuracies of the platform are tested using grating length gauges. Motion strokes of the parallel mechanism are measured using laser tracker.

## Keywords

Parallel platform, Offset RR-joint, Inverse kinematics, 6-P-RR-R-RR kinematic chains

Date received: 17 June 2018; accepted: 26 September 2018

## Introduction

A parallel platform consisting of several closed-form kinematic chains has several advantages over an open-form serial architecture, such as a simple structure, high specific stiffness, high load capacity, and noncumulative errors. The disadvantages of a parallel architecture are obvious, such as lower dexterity, a smaller workspace, and complex kinematics and dynamics problems.

In 1956, the Gough machine was originally proposed as a parallel structure that was utilized in testing of airplane tires.<sup>1</sup> In 1965, the Stewart machine was used as a flight simulator.<sup>2</sup> Thereafter, certain parallel mechanisms were developed in the field of robotics.<sup>3</sup> In the past two decades, applications of the parallel mechanism have garnered considerable interest. Practical applications of the parallel mechanism include motion simulators such as flight simulators,<sup>2–5</sup> a shaking platform that is used to test the seismic resistance of building architectures,<sup>6</sup> a six-degree-of-freedom(6-DOF) micro-vibration simulator,<sup>7</sup> a vibration isolation system for space optical payloads,<sup>8</sup> solar trackers,<sup>9,10</sup> industrial assembly

robots,<sup>11</sup> a polishing technique involving a serial–parallel mechanism,<sup>12</sup> force and torque sensors,<sup>13</sup> and even some entertainment devices.<sup>14</sup> Further, flexure-based parallel mechanisms, which are usually driven by piezoelectric actuators, are playing increasingly important roles in frontier applications where ultra-precision motion is required, for example, in the ultraviolet nanoimprint lithography(UV-NIL) process, optical fiber alignment, biological cell surgery, atomic force microscopy, and scanning electron microscopy.<sup>15–20</sup> A microelectromechanical system (MEMS)-based precision manipulator has also been used in a transmission electron microscope.<sup>21</sup>

<sup>1</sup>Changchun Institute of Optics, Fine Mechanics and Physics, Chinese Academy of Sciences, Changchun, Jilin, China

<sup>2</sup>Department of Mechanical Manufacture and Automation, University of Chinese Academy of Sciences, Beijing, China

### Corresponding author:

Zhen-bang Xu, Changchun Institute of Optics, Fine Mechanics and Physics, Chinese Academy of Sciences, No.3888, Dong Nanhu Road, Changchun 130033, China.

Email: xuzhenbang@gmail.com

In recent years, research efforts have been directed toward the application of parallel robots in surgery tools; displacement systems; and minimally invasive surgeries,<sup>22</sup> such as brain surgery,<sup>23</sup> laparoscopic surgery,<sup>24</sup> spine surgery,<sup>25</sup> orthopedic surgery,<sup>26</sup> and eye surgery.<sup>27</sup> Parallel architectures have also been investigated and utilized as secondary mirror adjustment mechanisms for large-aperture telescopes such as the Large Synoptic Survey Telescope (LSST),<sup>28</sup> the Thirty Meter Telescope (TMT),<sup>29</sup> and the Schwarzschild–Couder (SC) medium-sized candidate telescope.<sup>30</sup>

Research efforts toward a theoretical analysis of the kinematics of parallel architectures have led to long-term developments in recent years. Several previous works studied the inverse kinematics problem, which involves determination of a set of limb lengths or actuator displacements for a given position and orientation of a mobile platform.<sup>31–34</sup> Furthermore, some works investigated the forward kinematics problem, which entails determination of the position and orientation of a mobile platform for a set of given limb lengths or actuator displacements.<sup>35–37</sup> Generally, the forward kinematics problem of parallel mechanisms is more complicated than their inverse kinematics problem. This is in contrast to the case of serial-chain manipulators. Some works also investigated workspace characteristics, optimization design, error analysis, and kinematic calibration of parallel mechanisms.<sup>38–41</sup>

In related literature, R, U, S, C, and F denote a revolute pair, a universal joint, a spherical joint, a cylindrical pair, and a flexure joint, respectively; further,  $\underline{C}$  and  $\underline{P}$  denote, respectively, a cylindrical pair whose axial translation is actuated and an actuated prismatic pair. This paper presents a novel 6-DOF parallel platform with 6- $\underline{P}$ -RR-R-RR kinematic chains. The parallel platform adopts offset RR-joints instead of the traditional U-joints. The parallel structure is different from the usual three-legged 6-DOF parallel mechanisms: 3-RRPS chains,<sup>42</sup> 3-RPSR chains,<sup>43</sup> 3-RPRS chains,<sup>44</sup> 3-PRPS chains,<sup>45</sup> 3-3-PSPR chains,<sup>46</sup> 3-PPSP chains,<sup>47</sup> and 3-RRRS chains.<sup>48</sup> And it is also different from the common six-legged 6-DOF parallel mechanisms: 6-SPS chains<sup>2</sup> (this type of mechanisms is usually called a Stewart platform), 6-UPS chains<sup>49</sup> (this type of mechanisms is the most frequently used in applications, and is usually called as a Gough platform or a Hexapod), 6-PUS chains<sup>50</sup> (the first example of such architecture), 6-RUS chains<sup>51,52</sup> (this type of chain was first presented by Hunt), 6-UCU chains,<sup>53</sup> 6-RRCRR chains,<sup>31,32,54</sup> 6-PFF chains,<sup>34</sup> and other 6-DOF parallel platform with miscellaneous chains.<sup>55–57</sup>

The kinematics of common parallel mechanisms with traditional U-joints is relatively simple and straightforward owing to their zero offsets. Ji and Wu<sup>58</sup> and Hu and Lu<sup>59</sup> studied the kinematics of the offset 3- $\underline{U}$  $\underline{P}$  $\underline{U}$  and 3-RR- $\underline{P}$ -RR parallel architectures, respectively. Because of the existence of an

offset distance between the two non-intersecting axes of RR-joints, the kinematics of parallel architectures is more complicated. Dalvand and Shirinzadeh<sup>31</sup> and Dalvand et al.<sup>32</sup> studied the kinematics of offset 6- $\underline{U}$  $\underline{C}$  $\underline{U}$  parallel manipulators and 6-RRCRR parallel manipulators, respectively, which were used in a skull surgery system. Yu et al. studied the 6-RR- $\underline{R}$  $\underline{P}$ -RR parallel configuration, which is used as a positioning system of the secondary mirror of an optical telescope.<sup>54</sup> Manufacturing tolerances, installation errors and kinematic linkage offsets cause deviations in kinematic solutions of the traditional Stewart platform. Wang and Masory<sup>60</sup> investigated the inverse and forward kinematics of a 6- $\underline{U}$  $\underline{P}$  $\underline{S}$  parallel structure by numerical method. The solution was obtained by solving the inverse kinematic problem for each joint-link chain, treated as a RR- $\underline{P}$ -RRR serial robot, which took into account offsets introduced in U-joint and S-joint by manufacturing process and installation. David Daney presented three different calibration methods with a 6- $\underline{U}$  $\underline{P}$  $\underline{S}$  parallel platform using external measurement, additional redundant sensors or both in reference.<sup>61</sup> Daney assumed that S-joint was perfect, and U-joint and S-joint were perfectly mounted to the prismatic actuators. The U-joint defects were modeled by two kinematic parameters for each leg: the angle and the distance between the axes of the two revolute joints. In order to improve the motion accuracy as well as workspace and stiffness of the parallel mechanisms, three possible eccentricity types have been discussed as an alternative approach to conventional U-joints.<sup>62</sup> Such an eccentric design makes joint components more compact and stiffer, and makes pivoting range of joint larger. However, this method entails some challenges. Joint eccentricity acts as a lever and causes undesired bending moments and the kinematic transformation becomes more complex.

This novel 6- $\underline{P}$ -RR-R-RR parallel platform with offset RR joints is mainly used as the third mirror adjustment system of a large space telescope. In order to meet the special design requirements of a space optical system, the parallel platform should have high step precision, large load–size ratio, large workspace and high stiffness in both the transverse and the vertical directions.

In the interest of relatively large workspace and reduced risk of collision between the links, the parallel platform adopts offset RR-joints, although the kinematics of such a parallel platform becomes more complicated than that of the conventional platform because of the additional joint variables introduced by the offset joints.<sup>60–62</sup> The offset RR-joint is easier to manufacture than the U-joint and is not restricted by geometric configuration.<sup>62</sup> The offset design of joint makes pivoting range of joint larger and also makes the parallel structure more stiffer than traditional 6- $\underline{S}$  $\underline{P}$  $\underline{S}$ , 6- $\underline{U}$  $\underline{C}$  $\underline{U}$ , and 6- $\underline{U}$  $\underline{P}$  $\underline{S}$  configurations.<sup>62,63</sup> At the same time, the driving components of the structure are installed on the static platform, and the vertical dimension of the whole mechanism becomes

smaller, and the force transmission path is more conducive to improving the lateral stiffness. Such a structure possesses the advantages of having a very low center of mass, a very light moving mass. In addition, driving components are installed on the  $30^\circ$  slopes to improve the focus range.

This study examines the inverse kinematics problem of the novel 6-DOF parallel platform with 6-P-RR-R-RR kinematic chains. A solution of the inverse kinematics problem of this special family of parallel platforms is developed in this study. The accuracy and effectiveness of the proposed mathematical approach are verified by numerical simulations. The initial position of the platform is determined by a precision measuring arm. The motion resolutions and positioning accuracies of the platform are tested using grating length gauges, and then motion strokes of the parallel mechanism are measured using laser tracker. The rest of this paper is structured as follows. The structural design and parameters of the parallel architecture are explained in the Structural design section and the Parameters of parallel architectures section. Derivation of an inverse kinematics mathematical model and development of a numerical iterative solution are presented in the Inverse kinematics section. A numerical simulation is presented in the Numerical simulation section. Construction of the test system, inverse solution test and measurement of the movement performance of the parallel platform are described in the Test study section. Finally, the paper is concluded in the Conclusions section.

## Structural design

The special 6-DOF parallel platform presented in this paper is used as the third mirror adjustment system of a large space optical detector. The configuration and structural components of the parallel platform are shown in Figure 1.

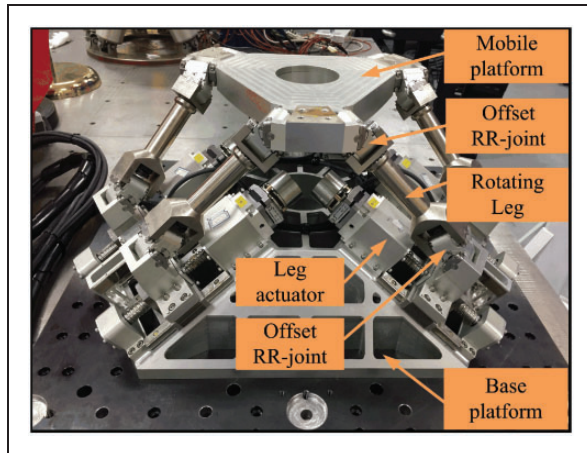


**Figure 1.** Configuration and structural components of parallel platform.

The parallel platform is composed mainly of a mobile platform (see Figure 2), a base platform (see Figure 3), six rotating legs, six leg actuators and 12 offset joints that connect the mobile platform, legs, and leg actuators. The lengths of the rotating legs are constant, and the motion of the lower offset joints is driven by leg actuators.

As shown in Figure 4, the leg actuator is composed of a brake, an electric motor, a high precision, no backlash harmonic reducer (Harmonic, HDUC-11 series, reduction ratio 100), a ball screw and preloaded nut (precision grade C2, pitch 4mm), two high precision, high stiffness parallel guides (THK, HSR12R1C1ME+110LPM-II series), and a slider that is connected to the screw nut. The lower joint is installed on the slider. When the motor runs, the leg actuator can drive the movement of the lower joint. A grating ruler (Renishaw, RELA130series, precision  $\pm 1 \mu\text{m}$ , subdivision error  $\pm 40 \text{ nm}$ ) and its reading head (Renishaw, RL26BAE050D50A series, resolution 50 nm) are fixed on the base platform and the slider, respectively; as a result, the position of the slider can be measured in real time. The six leg actuators are installed on the base platform as independent modules.

The number of DOFs of the parallel platform can be calculated using the Kutzbach–Grübler formula, as follows

$$F = 6(n - g - 1) + \sum_{i=1}^g f_i \quad (1)$$

where  $F$  is the number of DOFs of given mechanism;  $n$  is the total number of components;  $g$  is the total number of kinematic pairs; and  $f_i$  is DOFs of  $i$ -th kinematic pair.

It can be seen from Figure 1 that the total number of components in the parallel platform is 20; there are a total of 24 kinematic pairs, including 12 offset joints with two rotational DOFs, six rotating legs with one rotational DOF, and six sliding pairs with one DOF. Upon substitution of these values into equation (1), the number of DOFs of the parallel mechanism can be calculated to be six.

## Parameters of parallel architectures

The mobile platform of the parallel structure is connected to the leg actuators through the upper joints, supporting legs, and lower joints, wherein the supporting legs have a fixed length and only rotational freedom. Different from the conventional configuration of the parallel platform, the characteristics of this 6-P-RR-R-RR parallel mechanism presented in this paper are that it uses offset RR-joints. In such an offset joint, the centers of rotation of the two rotating pairs do not intersect and an offset distance exists between the two rotating axes. Furthermore, these

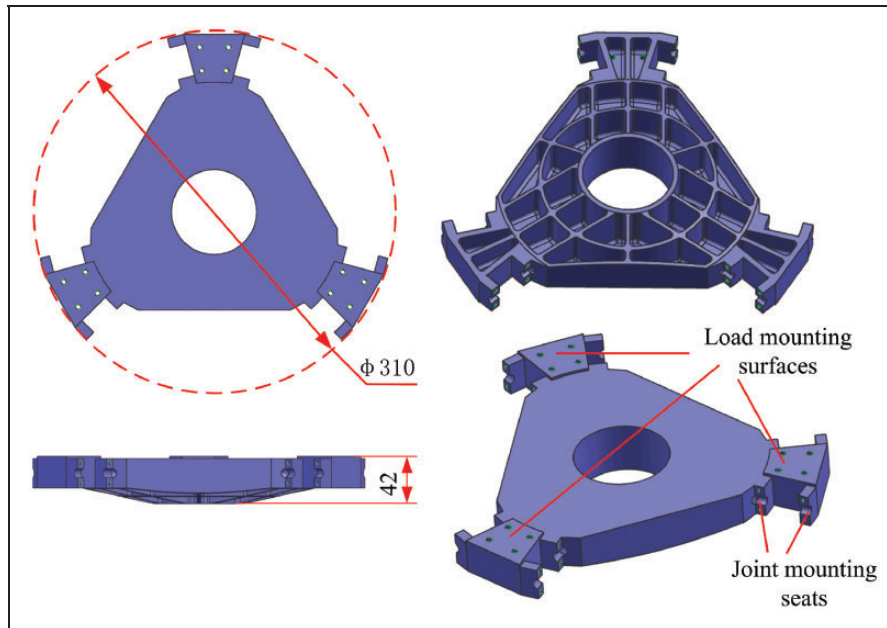


**Figure 2.** Structure of the mobile platform.

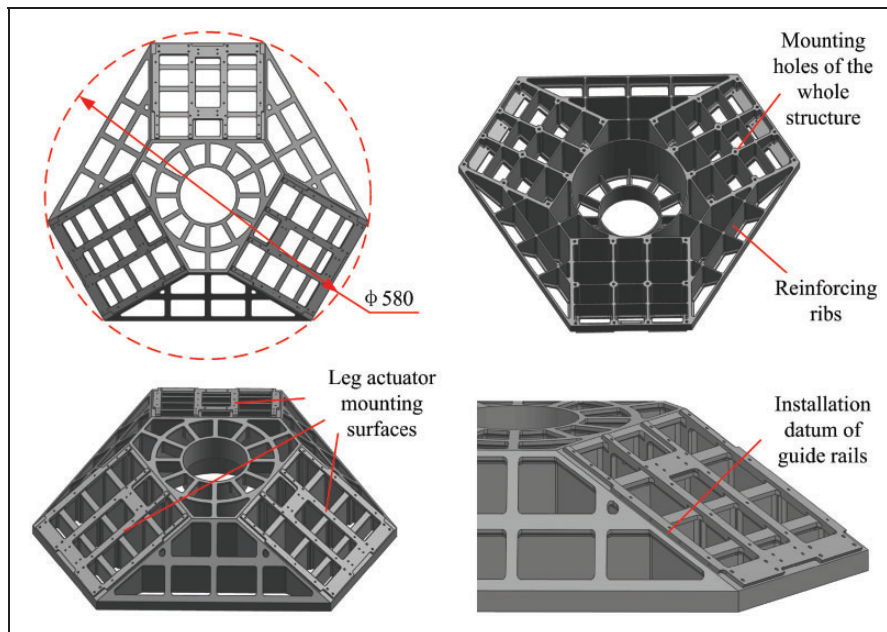


**Figure 3.** Structure of the base platform.

axes are perpendicular to each other, as shown in Figure 5(a) and (b).

Each lower joint is connected to the slider, which performs a straight-line driving motion along two inclined guides that form a  $30^\circ$  angle with the horizontal plane.

Because of the presence of offset RR-joints, two joint variables are introduced into each  $\underline{P}$ -RR-R-RR kinematic chain, as shown in Figure 5(c). Therefore, it is difficult to solve the inverse kinematics problem using the conventional kinematics method. In order to analyze the kinematics of the 6- $\underline{P}$ -RR-R-RR

parallel platform considered in this study, the schematic of the kinematic chain of the  $i$ -th leg is explained, as shown in Figure 6.

In order to describe the motion of the upper platform (the mobile platform), a global coordinate system  $O_B - X_B Y_B Z_B$  is set up at the center of the base of the lower platform (the static platform). The body frame  $O_P - X_P Y_P Z_P$  is set up at the center of the top surface of the mobile platform. The connecting line of six joint points  $P_i (i=1, \dots, 6)$  on the mobile platform forms a hexagon with a symmetrical distribution of  $120^\circ$ . These six points are also

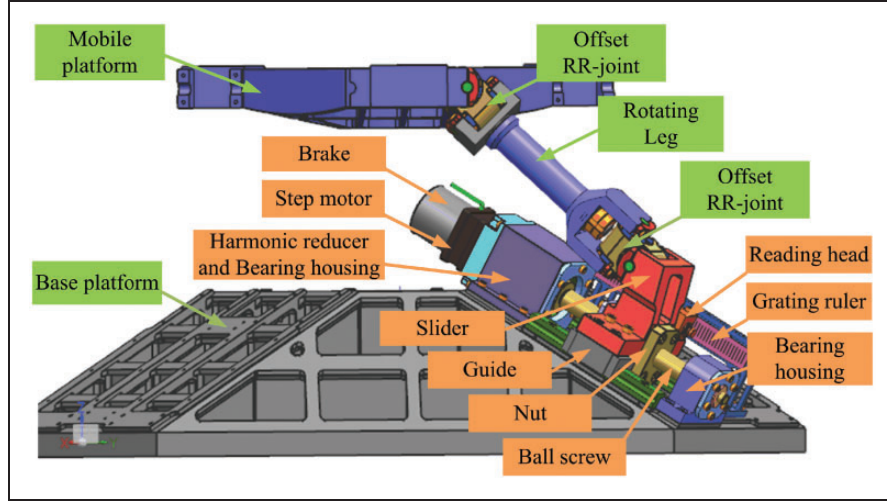


**Figure 4.** Components of the leg actuator.

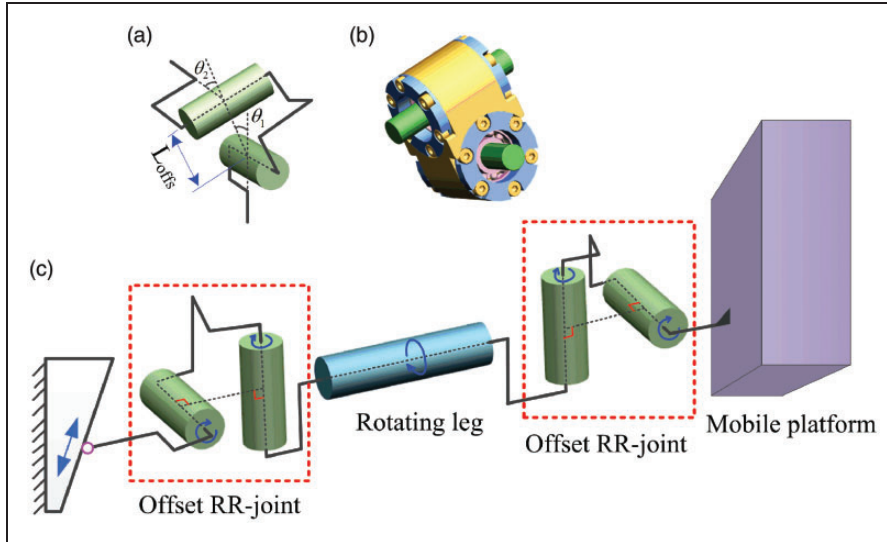


**Figure 5.**  $\underline{P}$ -RR-R-RR kinematic chain: (a) Schematic of offset RR-joint, (b) 3D model of offset RR-joint, and (c)  $\underline{P}$ -RR-R-RR kinematic chain.

distributed along the circumference of circle  $O'_P$ , whose radius is  $R_P$ . The distribution angle of the two upper joints is  $\theta_P$ . When the upper platform is at the zero position, the connecting line of the six lower joint points ( $i=1, \dots, 6$ ) also forms a hexagon with asymmetrical distribution of  $120^\circ$ . These lower joint points are also distributed along the circumference of circle  $O'_B$ , whose radius is  $R_B$ . The distribution angle of the two lower joints is  $\theta_B$ . The center of circle  $O'_P$  is located just below point  $O_P$ , and the distance between  $O'_P$  and  $O_P$  is  $H_P$ . The center of circle  $O'_B$  is located just above point  $O_B$ , and the distance between  $O'_B$  and  $O_B$  is  $H_B$ . The offset distances of the upper and lower joints are denoted as  $L_{UP_i}$  and  $L_{UB_i}$ , respectively. In addition,  $\theta_Q$  denotes the angle between the movement direction of the lower joint point  $B_i$  and the horizontal surface.  $S_i$  denotes the displacement of the lower joint point along the guide.

The geometrical parameters of the parallel platform are listed in Table 1.

Because of the presence of the offset joints, three additional sets of coordinates are needed to set up, as shown in Figure 7. Based on the global coordinate system, the local coordinate systems  $B_{i0} - X_{B_{i0}} Y_{B_{i0}} Z_{B_{i0}}$  ( $i=1, \dots, 6$ ) are established, as shown in Figure 7(a). When the upper platform is located at its zero position, the lower joints remain at points  $B_{i0}$  ( $i=1, \dots, 6$ ).  $X_{B_{i0}}$  is directed along the joint shaft, and  $Z_{B_{i0}}$  is directed vertically upward. The second set of coordinates,  $B_i - X_{B_i} Y_{B_i} Z_{B_i}$  ( $i=1, \dots, 6$ ), is connected to the lower joints; this set of coordinates can be obtained by translation of the coordinate systems  $B_{i0} - X_{B_{i0}} Y_{B_{i0}} Z_{B_{i0}}$  ( $i=1, \dots, 6$ ) and translation of the coordinate origins  $B_i$  ( $i=1, \dots, 6$ ) along the guides. The third set of coordinates,  $P_i - X_{P_i} Y_{P_i} Z_{P_i}$  ( $i=1, \dots, 6$ ), is connected to the joint installation



joints. The length of the  $i$ -th leg ( $L_i$ ) is defined as the distance between points  $U_{B_i}$  and  $U_{P_i}$ . Parameter  $\psi_{B_i}$  is the angle between the  $Y_{B_i}$  axis and line  $B_i U_{B_i}$ . Parameter  $\psi_{P_i}$  is the angle between the  $Y_{P_i}$  axis and line  $U_{P_i} P_i$ . Both  $\psi_{B_i}$  and  $\psi_{P_i}$  are joint variables.

According to the symmetry and definition of local coordinate systems, the coordinates of point  $B_{i0}$  in the global frame  $O_B - X_B Y_B Z_B$  are expressed as follows:

$${}^{O_B}B_{i0} = [R_B \cdot \cos \theta_{B_{i0}} \quad R_B \cdot \sin \theta_{B_{i0}} \quad H_B]^T \quad (2)$$

where  $\theta_{B_{i0}} = \frac{\pi}{3}i - \frac{\theta_P}{2}$  ( $i = 1, 3, 5$ ) and  $\theta_{B_{i0}} = \frac{\pi}{3}(i-1) + \frac{\theta_P}{2}$  ( $i = 2, 4, 6$ )

In the frame  $O_P - X_P Y_P Z_P$ , the coordinates of the upper joint point  $P_i$  are expressed as follows

$${}^{O_P}P_i = [R_P \cdot \cos \theta_{P_i} \quad R_P \cdot \sin \theta_{P_i} \quad -H_P]^T \quad (3)$$

where  $\theta_{P_i} = \frac{\pi}{3}i - \frac{\theta_P}{2}$  ( $i = 1, 3, 5$ ) and  $\theta_{P_i} = \frac{\pi}{3}(i-1) + \frac{\theta_P}{2}$  ( $i = 2, 4, 6$ )

When the global frame  $O_B - X_B Y_B Z_B$  rotates by angle  $\theta'_i$  counterclockwise about the  $Z_B$  axis, its  $X_B$  axis is parallel to the  $X_{B_{i0}}$  axis of the local coordinate system  $B_{i0} - X_{B_{i0}} Y_{B_{i0}} Z_{B_{i0}}$  in the same direction. When  $i = 1, 6$ ,  $\theta'_i = \frac{\pi}{2}$ ; when  $i = 2, 3$ ,  $\theta'_i = \frac{7\pi}{6}$ ; and when  $i = 4, 5$ ,  $\theta'_i = \frac{11\pi}{6}$ .

The transformation matrix  ${}^{O_B}T_{B_{i0}}$  from the local coordinate system  $B_{i0} - X_{B_{i0}} Y_{B_{i0}} Z_{B_{i0}}$  for the lower joint points at the zero position to the global coordinate system  $O_B - X_B Y_B Z_B$  can be expressed as follows

$${}^{O_B}T_{B_{i0}} = \begin{bmatrix} c\theta'_i & -s\theta'_i & 0 & R_B c\theta_{B_{i0}} \\ s\theta'_i & c\theta'_i & 0 & R_B s\theta_{B_{i0}} \\ 0 & 0 & 1 & H_B \\ 0 & 0 & 0 & 1 \end{bmatrix} \quad (4)$$

where  $s(\cdot) = \sin(\cdot)$  and  $c(\cdot) = \cos(\cdot)$ ; the same notation applies to subsequent matrices.

$S_i$  denotes the displacement of the lower joint point  $B_i$  along the guide. When  $B_i$  moves upward along the guide, the value of  $S_i$  is positive. The transformation matrix from the moving coordinate system  $B_i - X_{B_i} Y_{B_i} Z_{B_i}$  connected to the slider to the local coordinate system  $B_{i0} - X_{B_{i0}} Y_{B_{i0}} Z_{B_{i0}}$  can be expressed as

$${}^{B_{i0}}T_{B_i} = \begin{bmatrix} 1 & 0 & 0 & 0 \\ 0 & 1 & 0 & S_i c\theta_Q \\ 0 & 0 & 1 & S_i s\theta_Q \\ 0 & 0 & 0 & 1 \end{bmatrix} \quad (5)$$

The transformation matrix  ${}^{O_P}T_{P_i}$  from the local coordinate system  $P_i - X_{P_i} Y_{P_i} Z_{P_i}$  to the moving coordinate system  $O_P - X_P Y_P Z_P$  connected to the

upper platform can be expressed as

$${}^{O_P}T_{P_i} = \begin{bmatrix} c\theta_{P_i} & -s\theta_{P_i} & 0 & R_P c\theta_{P_i} \\ s\theta_{P_i} & c\theta_{P_i} & 0 & R_P s\theta_{P_i} \\ 0 & 0 & 1 & -H_P \\ 0 & 0 & 0 & 1 \end{bmatrix} \quad (6)$$

In the moving coordinate system  $B_i - X_{B_i} Y_{B_i} Z_{B_i}$  connected to the slider, point  $U_{B_i}$  is expressed as

$${}^{B_i}U_{B_i} = [0 \quad L_{UB_i} \cdot c\psi_{B_i} \quad L_{UB_i} \cdot s\psi_{B_i} \quad 1]^T \quad (7)$$

In the coordinate system  $P_i - X_{P_i} Y_{P_i} Z_{P_i}$ , point  $U_{P_i}$  is expressed as

$${}^{P_i}U_{P_i} = [0 \quad L_{UP_i} \cdot c(\pi + \psi_{P_i}) \quad L_{UP_i} \cdot s(\pi + \psi_{P_i}) \quad 1]^T \quad (8)$$

The upper and lower platforms, the legs, and the joints are assumed to have high rigidity. The pose of the upper platform (moving frame  $O_P - X_P Y_P Z_P$ ) in the global frame  $O_B - X_B Y_B Z_B$  is determined by a six-dimensional vector  $[X, Y, Z, \alpha, \beta, \gamma]^T$ . In this vector,  $X$ ,  $Y$ , and  $Z$  denote the coordinates of point  $O_P$  in the global frame  $O_B - X_B Y_B Z_B$  and  $\alpha$ ,  $\beta$ , and  $\gamma$  denote the successive rotations of the moving frame  $O_P - X_P Y_P Z_P$  about the global coordinate axes  $X_B$ ,  $Y_B$ , and  $Z_B$ , respectively, in the specific order  $X - Y - Z$ . Specifically,  $\alpha$  denotes the angle of yaw motion about the  $X_B$  axis,  $\beta$  denotes the angle of pitch about the  $Y_B$  axis, and  $\gamma$  denotes the angle of roll motion about the  $Z_B$  axis. The transformation matrix  ${}^{O_B}T_{O_P}$  from the moving coordinate system  $O_P - X_P Y_P Z_P$  to the global coordinate system  $O_B - X_B Y_B Z_B$  can be expressed as

$${}^{O_B}T_{O_P} = \begin{bmatrix} c\beta c\gamma & -c\beta s\gamma & s\beta & X \\ c\alpha \gamma + s\alpha s\beta c\gamma & c\alpha \gamma - s\alpha s\beta s\gamma & -s\alpha c\beta & Y \\ s\alpha \gamma - c\alpha s\beta c\gamma & s\alpha \gamma + c\alpha s\beta s\gamma & c\alpha c\beta & Z \\ 0 & 0 & 0 & 1 \end{bmatrix} \quad (9)$$

## Inverse kinematics

The inverse kinematics problem of this kind of 6-DOF parallel platform is to determine the slider displacements of the six leg actuators when the pose vector  $[X, Y, Z, \alpha, \beta, \gamma]^T$  of the mobile platform is given. As the upper platform is not at the zero position, the six lower joint points  $B_i (i = 1, \dots, 6)$  may not necessarily satisfy the coplanar conditions. For the parallel structure shown in Figure 6, the vector of the  $i$ -th leg satisfies the following equation

$$|L_i| = |{}^{B_i}U_{B_i} U_{P_i}| = L_i \quad (10)$$

For a given pose of the mobile platform, three unknown variables (lower-joint slider displacement  $S_i$  and upper and lower joint variables  $\psi_{B_i}$  and  $\psi_{P_i}$ ) are included in equation (10). At present, only one equation including three unknown variables is established for each leg. In order to solve all 18 unknown variables of the six legs, two more kinematic constraint equations are required for each leg. This makes solving of the inverse kinematics problem of the parallel mechanism with offset joints more complicated than that of the parallel mechanism with conventional universal joints.

According to the characteristics of the offset joint, in the coordinate system  $B_i - X_{B_i} Y_{B_i} Z_{B_i}$ , line  $B_i U_{B_i}$  is collinear with the projection line of line  $U_{B_i} U_{P_i}$  in the  $Y_{B_i} Z_{B_i}$  plane. That is, in the  $Y_{B_i} Z_{B_i}$  plane, the angle between line  $B_i U_{B_i}$  and the  $Y_{B_i}$  axis is always the same as the angle between line  $U_{B_i} U_{P_i}$  and the  $Y_{B_i}$  axis. Similarly, in the coordinate system  $P_i - X_{P_i} Y_{P_i} Z_{P_i}$ , line  $U_{P_i} P_i$  is collinear with the projection line of line  $U_{B_i} U_{P_i}$  in the  $Y_{P_i} Z_{P_i}$  plane, as shown in Figure 8.

From the analysis of characteristics of the offset joints, two relations can be established

$$\tan(\psi_{B_i}) = \frac{{}^{B_i}Z_{L_i}}{{}^{B_i}Y_{L_i}} \quad (11)$$

$$\tan(\psi_{P_i}) = \frac{{}^{P_i}Z_{L_i}}{{}^{P_i}Y_{L_i}} \quad (12)$$

where  ${}^{B_i}Z_{L_i}$  and  ${}^{B_i}Y_{L_i}$  are components of vector  ${}^{B_i}U_{B_i}U_{P_i}$  along the  $Y_{B_i}$  and  $Z_{B_i}$  directions, respectively, and  ${}^{P_i}Z_{L_i}$  and  ${}^{P_i}Y_{L_i}$  are components of vector  ${}^{P_i}U_{B_i}U_{P_i}$  along the  $Y_{P_i}$  and  $Z_{P_i}$  directions, respectively.

According to the coordinate transformation relation, the vector  ${}^{B_i}U_{B_i}U_{P_i}$  of the  $i$ -th leg can be expressed as

$$\begin{aligned} {}^{B_i}L_i &= {}^{B_i}U_{B_i}U_{P_i} = {}^{B_i}U_{P_i} - {}^{B_i}U_{B_i} \\ &= {}^{B_i}T_{B_{i0}} {}^{B_{i0}}T_{O_B} {}^{O_B}T_{O_P} {}^{O_P}T_{P_i} {}^{P_i}U_{P_i} - {}^{B_i}U_{B_i} \quad (13) \\ &= {}^{B_{i0}}T_{B_i}^{-1} {}^{O_B}T_{B_i}^{-1} {}^{O_B}T_{O_P} {}^{O_P}T_{P_i} {}^{P_i}U_{P_i} - {}^{B_i}U_{B_i} \end{aligned}$$

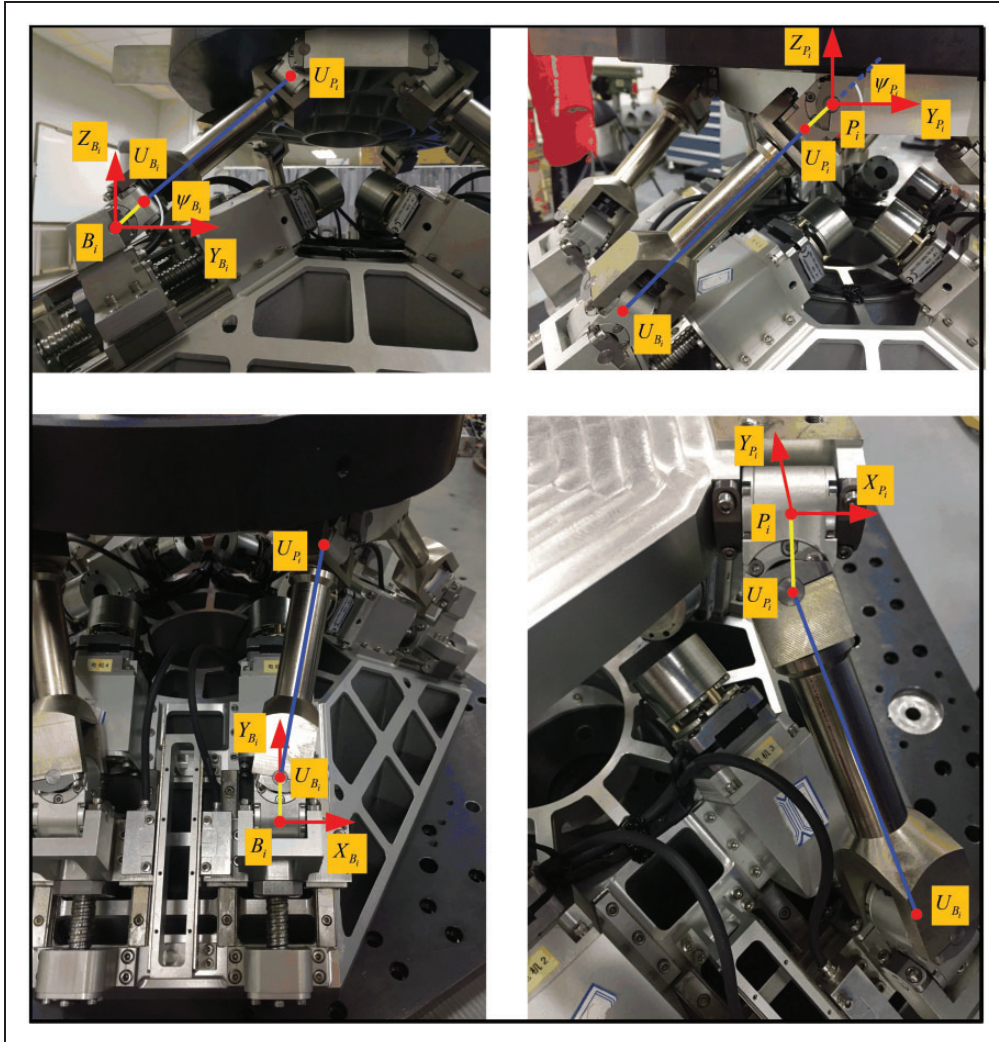


Figure 8. Kinematic constraints of offset RR-joints.

Similarly, the vector  ${}^P U_{B_i} U_{P_i}$  of the  $i$ -th leg can be expressed as

$$\begin{aligned} {}^P L_i &= {}^P U_{B_i} U_{P_i} = {}^P U_{P_i} - {}^P U_{B_i} \\ &= {}^P U_{P_i} - {}^P T_{O_P} {}^O_P T_{O_B} {}^O_B T_{B_{i0}} {}^{B_{i0}} T_{B_i} {}^{B_i} U_{B_i} \quad (14) \\ &= {}^P U_{P_i} - {}^O_P T_{P_i}^{-1} {}^O_B T_{O_P} {}^O_B T_{B_{i0}} {}^{B_{i0}} T_{B_i} {}^{B_i} U_{B_i} \end{aligned}$$

Because  ${}^{B_i} Z_{L_i}$ ,  ${}^{B_i} Y_{L_i}$ ,  ${}^{P_i} Z_{L_i}$ , and  ${}^{P_i} Y_{L_i}$  all contain joint-angle variables  $\psi_{P_i}$  and  $\psi_{B_i}$  and slider displacement  $S_i$  of the leg actuator, equations (11) and (12) can be rewritten as, respectively,

$$\frac{\sin(\psi_{B_i})}{\cos(\psi_{B_i})} = \frac{a_1 \cdot \sin(\psi_{P_i}) + a_2 \cdot \sin(\psi_{B_i}) + a_3 \cdot S_i + a_4}{b_1 \cdot \cos(\psi_{P_i}) + b_2 \cdot \cos(\psi_{B_i}) + b_3 \cdot S_i + b_4} \quad (15)$$

$$\frac{\sin(\psi_{P_i})}{\cos(\psi_{P_i})} = \frac{a_1 \cdot \sin(\psi_{P_i}) + a_2 \cdot \sin(\psi_{B_i}) + a_3 \cdot S_i + a_4}{c_1 \cdot \cos(\psi_{P_i}) + c_2 \cdot \cos(\psi_{B_i}) + c_3 \cdot S_i + c_4} \quad (16)$$

where  $a_i$  and  $b_i (i=1, \dots, 6)$  have constant values. Further, equations (15) and (16) can be rewritten in the following forms, respectively

$$\begin{aligned} c\psi_{B_i} \cdot (a_1 \cdot s\psi_{P_i} + a_2 \cdot s\psi_{B_i} + a_3 \cdot S_i + a_4) - s\psi_{B_i} \\ \cdot (b_1 \cdot c\psi_{P_i} + b_2 \cdot c\psi_{B_i} + b_3 \cdot S_i + b_4) = 0 \end{aligned} \quad (17)$$

$$\begin{aligned} c\psi_{P_i} \cdot (a_1 \cdot s\psi_{P_i} + a_2 \cdot s\psi_{B_i} + a_3 \cdot S_i + a_4) - s\psi_{P_i} \\ \cdot (c_1 \cdot c\psi_{P_i} + c_2 \cdot c\psi_{B_i} + c_3 \cdot S_i + c_4) = 0 \end{aligned} \quad (18)$$

Equation (10) can be expressed as the following nonlinear equation

$$({}^{B_i} U_{B_i} U_{P_i})^T \cdot ({}^{B_i} U_{B_i} U_{P_i}) - L_i^2 = 0 \quad (19)$$

As the inverse kinematics problem involves the solution of a nonlinear equation set consisting of equations (17) to (19), the Newton–Raphson numerical iterative method is used to solve the problem. The nonlinear equation set that needs to be solved is defined as

$$\begin{cases} F_{i1}(\psi_{B_i}, \psi_{P_i}, S_i) = 0 \\ F_{i2}(\psi_{B_i}, \psi_{P_i}, S_i) = 0 \\ F_{i3}(\psi_{B_i}, \psi_{P_i}, S_i) = 0 \end{cases} \quad (20)$$

where functions  $F_{i1}$ ,  $F_{i2}$ , and  $F_{i3}$  correspond to the expressions on the left sides of the equality signs of equations (17) to (19), respectively.

Unknown variables  $\psi_{B_i}$ ,  $\psi_{P_i}$ , and  $S_i$  of the nonlinear equation set in equation (20) can be derived

using the following iterative format

$$\begin{aligned} \begin{bmatrix} \psi_{B_i} \\ \psi_{P_i} \\ S_i \end{bmatrix}_{(n+1)} &= \begin{bmatrix} \psi_{B_i} \\ \psi_{P_i} \\ S_i \end{bmatrix}_{(n)} \\ &- \begin{bmatrix} \frac{\partial F_{i1}}{\partial \psi_{B_i}} & \frac{\partial F_{i1}}{\partial \psi_{P_i}} & \frac{\partial F_{i1}}{\partial S_i} \\ \frac{\partial F_{i2}}{\partial \psi_{B_i}} & \frac{\partial F_{i2}}{\partial \psi_{P_i}} & \frac{\partial F_{i2}}{\partial S_i} \\ \frac{\partial F_{i3}}{\partial \psi_{B_i}} & \frac{\partial F_{i3}}{\partial \psi_{P_i}} & \frac{\partial F_{i3}}{\partial S_i} \end{bmatrix}_{(n)}^{-1} \cdot \begin{bmatrix} F_{i1} \\ F_{i2} \\ F_{i3} \end{bmatrix}_{(n)} \end{aligned} \quad (21)$$

In addition to establishment of the numerical iterative format, the initial values  $\psi_{B_i}^{(0)}$ ,  $\psi_{P_i}^{(0)}$ , and  $S_i^{(0)}$  should be provided for solving the nonlinear equation set. The selection of initial values is crucial to the convergence of iterations, the number of iterations, and the computational efficiency. The initial values should be close to the real values. According to the  $\underline{P}$ -RR-R-RR configuration,  $\psi_{B_i}$  is close to the angle between the projection vector of  $B_i P_i$  on the  $Y_{B_i} Z_{B_i}$  plane and the  $Y_{B_i}$  axis. Similarly,  $\psi_{P_i}$  is also close to the angle between the projection vector of  $B_i P_i$  on the  $Y_{P_i} Z_{P_i}$  plane and the  $Y_{P_i}$  axis. In other words, the initial angles  $\psi_{B_i}^{(0)}$  and  $\psi_{P_i}^{(0)}$  are defined as angles  $\psi_{B_i}$  and  $\psi_{P_i}$ , respectively, when the parallel platform adopts the 6- $\underline{P}$ URU architecture with conventional U-joints. The initial value of slider displacement,  $S_i^{(0)}$ , of the  $i$ -th leg actuator is taken as zero.

$$\psi_{B_i}^{(0)} = \arctan\left(\frac{{}^{B_i} Z_{B_i P_i}}{{}^{B_i} Y_{B_i P_i}}\right) \quad (22)$$

$$\psi_{P_i}^{(0)} = \arctan\left(\frac{{}^{P_i} Z_{B_i P_i}}{{}^{P_i} Y_{B_i P_i}}\right) \quad (23)$$

$$S_i^{(0)} = 0 \quad (24)$$

where  ${}^{B_i} Z_{B_i P_i}$  and  ${}^{B_i} Y_{B_i P_i}$  are components of vector  ${}^{B_i} B_i P_i$  along the  $Y_{B_i}$  and  $Z_{B_i}$  directions, respectively, and  ${}^{P_i} Z_{B_i P_i}$  and  ${}^{P_i} Y_{B_i P_i}$  are components of vector  ${}^{P_i} B_i P_i$  along the  $Y_{P_i}$  and  $Z_{P_i}$  directions, respectively.

In order to obtain convergence results of  $\psi_{B_i}$ ,  $\psi_{P_i}$ , and  $S_i$ , which satisfy given error conditions, numerical iterative computations are performed using the iterative format in equation (21) and the initial conditions in equations (22) to (24). Thus, the inverse kinematics problem of the 6- $\underline{P}$ -RR-R-RR parallel platform is solved. The flowchart of the numerical iterative solution of the inverse kinematics problem is shown in Figure 9.

## Numerical simulation

### Simulation of kinematics solution

In order to verify the accuracy of the numerical iterative algorithm of the inverse kinematics solution,

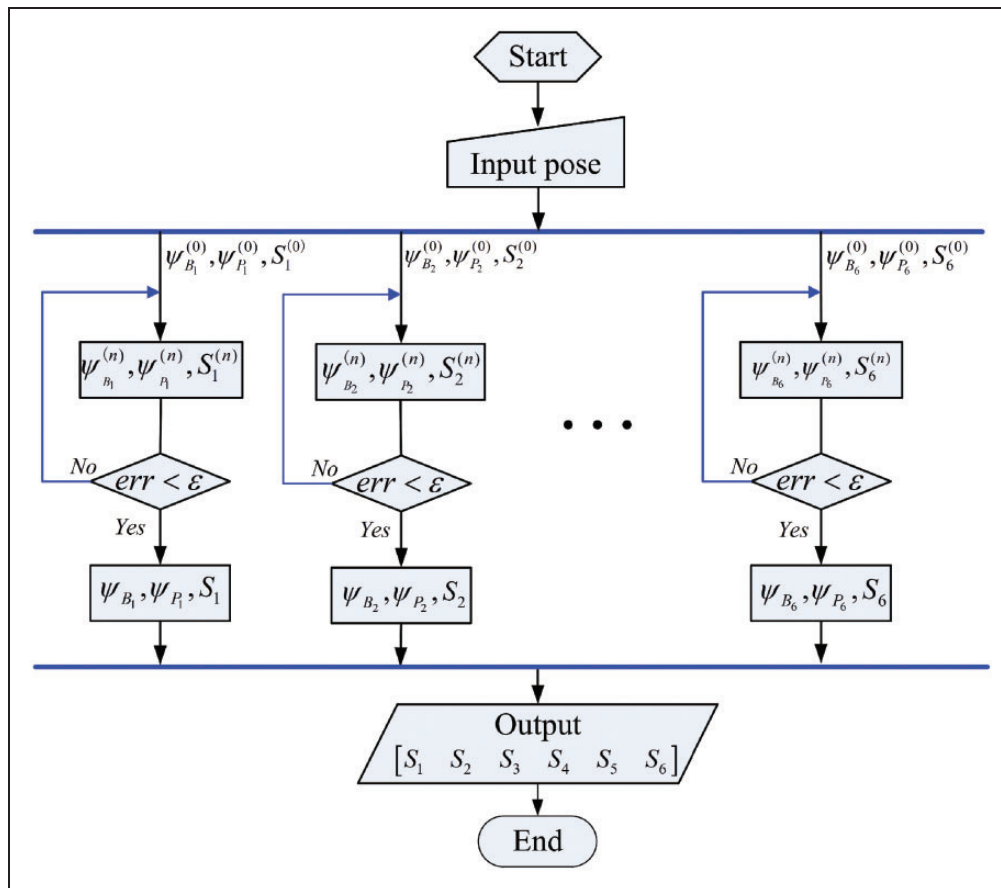


Figure 9. Flowchart of solution of inverse kinematics problem of parallel platform.

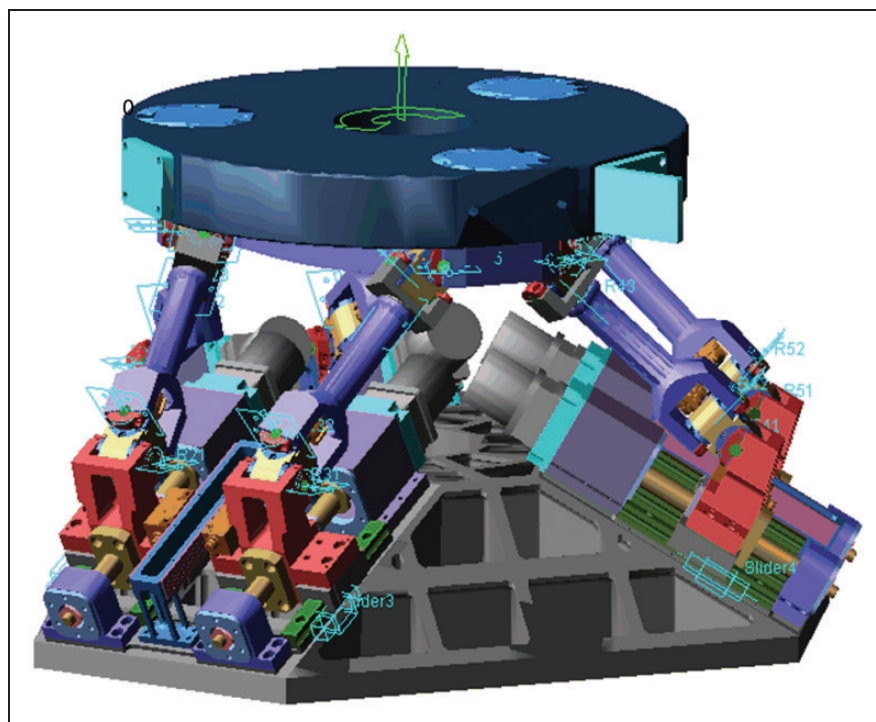


Figure 10. Kinematic model in ADAMS.

a kinematics simulation is performed in ADAMS. In the simulation process, all the components are set as rigid bodies. The kinematic model is shown in Figure 10.

Three arbitrary poses of the simulated load connected to the mobile platform (frame  $O_P - X_P Y_P Z_P$ ) with respect to frame  $O_B - X_B Y_B Z_B$  are selected randomly, as given in Table 2. The numerical iterative solutions of the inverse kinematics problems are determined using the forementioned algorithm outlined in Figure 9. In the ADAMS software, the mobile platform is moved to poses  $P_1$ ,  $P_2$ , and  $P_3$  separately, and the displacements of sliders driving the lower joints are measured. A comparison of the numerical iteration results and the simulation results is presented in Table 3.

It can be seen from Table 3 that the results of the numerical iterative calculations are in good agreement with the results of the numerical simulation and that the differences between these two sets of results are smaller than 0.02 mm. These differences are caused by the iterative control error. Therefore, the accuracy of the inverse kinematics iterative algorithm is verified by the numerical simulation.

### Simulation of slider speeds and displacements

Pose  $P_1$  is chosen as the target pose, and in the process of driving the parallel platform to  $P_1$ , the speed of the driving motors and slider of each leg actuator is simulated.

In each leg actuator, the stepper motor drives the lead screw to rotate through the harmonic reducer, so the lead screw nut drives the slider to move along the guides. In order to improve the motion resolution, the

step angle of the stepper motor is subdivided electronically, so the step size of the motor is calculated as follows

$$Step = \frac{1.8^\circ}{n_s} = \frac{1.8^\circ}{4} = 0.45^\circ \quad (25)$$

where  $n_s$  is the number of electronic subdivision.

The running speeds of the motors of six leg actuators are shown in Figure 11.

The acceleration of the six motors is equal in both accelerating and decelerating stages.

$$Acc_m = Dec_m = 2000 \times Step/s^2 = 2.5r/s^2 \quad (26)$$

Here  $Acc_m$  is the acceleration of the motor;  $Dec_m$  is the deceleration of the motor.

When these motors speed up to the maximum speeds, they enter the uniform motion stage. The maximum driving speeds of the six motors are

$$V_{m\_max} = 5000 \times Step/s = 6.25r/s \quad (27)$$

where  $V_{m\_max}$  is the maximum driving speeds of the six stepper motors.

According to the speed of the motor driving motion, the speed of the driving slider can be calculated by using the reduction ratio of the harmonic

**Table 2.** Arbitrary selected poses of mobile platform for numerical simulation.

Pose	X(mm)	Y(mm)	Z(mm)	$\alpha(^{\circ})$	$\beta(^{\circ})$	$\gamma(^{\circ})$
$P_1$	20	15	316	0	0	0
$P_2$	0	0	306	10	5	8
$P_3$	8	-13	302	8	-10	12

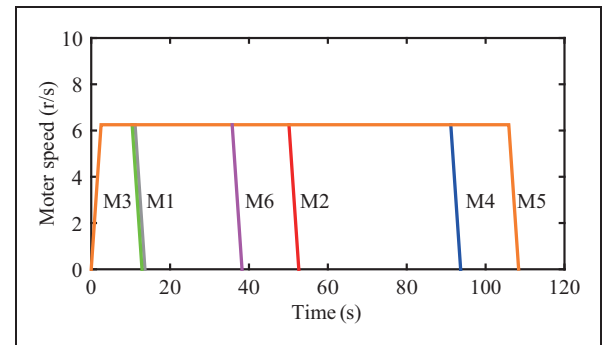


**Figure 11.** Motor speeds vs. time. M1: Motor1; M2: Motor2; M3: Motor3; M4: Motor4; M5: Motor5; M6: Motor6.

**Table 3.** Comparison of numerical iterative results and simulation results.

Slider displacement		$S_1$ (mm)	$S_2$ (mm)	$S_3$ (mm)	$S_4$ (mm)	$S_5$ (mm)	$S_6$ (mm)
$P_1$	<b>I</b>	-2.77906158	12.53348044	2.59413121	22.79236150	26.46862370	-8.93469354
$P_1$	<b>N</b>	-2.77906159	12.53348044	2.59413122	22.79236150	26.46862370	-8.93469354
$P_2$	<b>I</b>	28.67407391	-0.47165694	16.32753905	-2.79767668	2.80492154	-18.06510404
$P_2$	<b>N</b>	28.67407390	-0.47165694	16.32753906	-2.79767668	2.80492153	-18.06510403
$P_3$	<b>I</b>	23.35744913	9.22323450	11.30958958	-23.10067823	24.88490965	-20.97139081
$P_3$	<b>N</b>	23.35744912	9.22323450	11.30958958	-23.10067822	24.88490966	-20.97139081

**I:** Iterative algorithm; **N:** Numerical simulation.

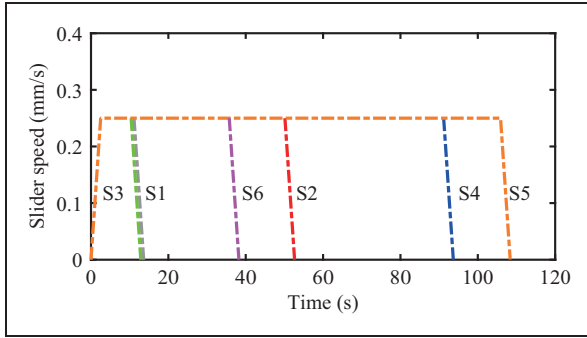


**Figure 12.** Slider speeds vs. time. S1: Slider1; S2: Slider2; S3: Slider3; S4: Slider4; S5: Slider5; S6: Slider6.

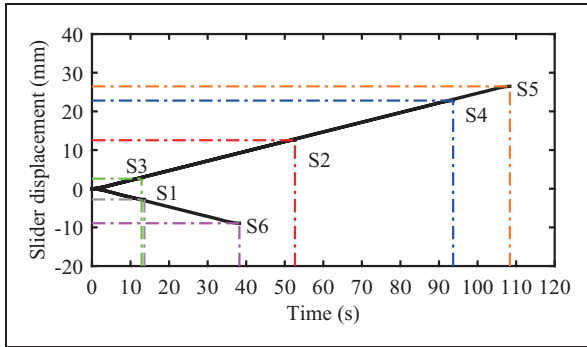


**Figure 13.** Displacements of the six sliders vs. time. S1: Slider1; S2: Slider2; S3: Slider3; S4: Slider4; S5: Slider5; S6: Slider6.

reducer and the pitch of the ball screw. The speed curves of the six sliders are shown in Figure 12.

As can be seen from the Figure 12, each slider does constant accelerating motion during the start-up stage and evenly decelerates at the end of the movement. The acceleration of the six sliders is equal in both accelerating and decelerating stages.

$$Acc_s = Dec_s = \frac{Acc_m \cdot P_h}{n_r} = 0.1 \text{ mm/s}^2 \quad (28)$$

Here  $Acc_s$  is acceleration of the slider;  $Dec_s$  is deceleration of the slider;  $n_r$  is reduction ratio of the harmonic reducer; and  $P_h$  is ball screw's pitch.

When the six sliders accelerate to their maximum speeds, they start to do uniform motion. The maximum speeds of the six sliders are

$$V_{s\_max} = \frac{V_{m\_max} \cdot P_h}{n_r} = 0.25 \text{ mm/s} \quad (29)$$

where  $V_{s\_max}$  is the maximum speed of the six sliders.

As shown in Figure 13, the relationship between displacements of six sliders and time is simulated. It can be seen from the diagram that when each slider is actuating the lower joint movement, the transition between different movement stages is gentle.

## Test study

### Initial position test

The initial position of the parallel platform is determined by the theoretical configuration of the

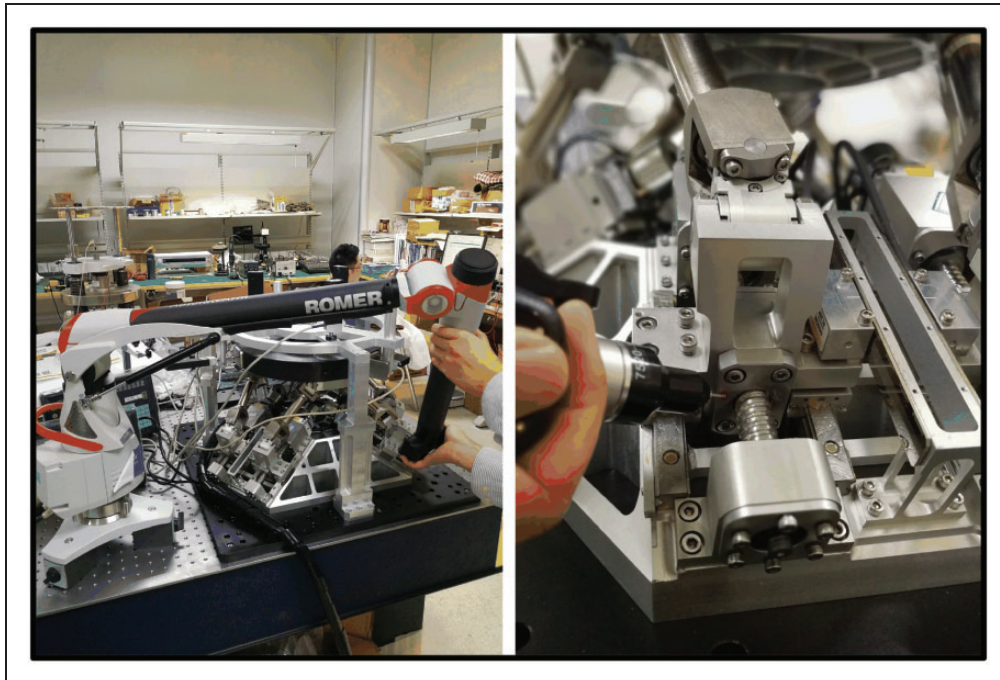


**Figure 14.** Measurement of the position of the screw nut.

platform, and the initial position is the reference position of the platform motion. After the assembly of the parallel platform, the initial position of the platform is determined by the initial position of 12 upper and lower offset joints. The initial position of upper six offset joints can be ensured by the machining precision of the mobile platform and the assembly precision of the upper offset joints. The initial position of the lower six offset joints can be indirectly determined by the precise position of the screw nut. As shown in Figure 14, in order to determine the position of the screw nut, a 6-DOF measuring arm (Romer arm, the measurement accuracy is  $10\mu\text{m}$  and the resolution is  $1\mu\text{m}$ ) is used to measure the distance between flange of the screw nut and the end face of the bearing seat.

### Inverse solution test

In order to verify the accuracy of the numerical iterative algorithm of the inverse kinematics solution, inverse solution of the parallel platform is tested in the real prototype. The test system constructed in this

study is composed mainly of a vibration isolation table, a test fixture, a simulated load, the designed parallel platform, grating length gauges, and digital display devices, as shown in Figure 15. The test system uses six grating length gauges: three to measure the three translational motions along the X, Y, and Z directions and the remaining three to measure three small-range rotational motions about the X, Y, and Z axes. The top three length gauges are mounted directly onto the disk-like test tool and the remaining three length gauges are mounted onto the clamps.

When target pose of the parallel platform is given, the displacement of each slider can be calculated using the inverse kinematics algorithm. Then, the driving steps corresponding to the displacement of each slider can be calculated by using the pitch of ball screw, the reduction ratio of the harmonic reducer and the step angle of the stepper motor. In order to satisfy the application needs of high precision and high-resolution capability, electronic subdivision method is used to subdivide the step angle of the stepper motor. An open loop control method is used to drive the slider in each motion cycle. After every motion cycle, the controller evaluates the position error of the slider according to the feedback value of the reading head of the grating ruler mounted on the slider. If there is slider position error caused by transmission clearance, pitch error of lead screw, etc., the number of motor driving steps that needs to be compensated is calculated and the motor is driven

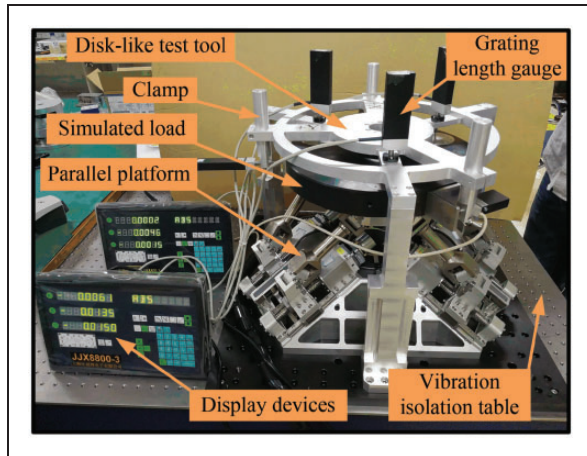


Figure 15. Configuration of the test system.

Table 4. Arbitrary selected poses of mobile platform for inverse solution test.

Pose	X(mm)	Y(mm)	Z(mm)	$\alpha$ (°)	$\beta$ (°)	$\gamma$ (°)
$P'_1$	3	10	311	0	0	0
$P'_2$	0	-10	306	0	3	0
$P'_3$	5	0	301	-3	0	0

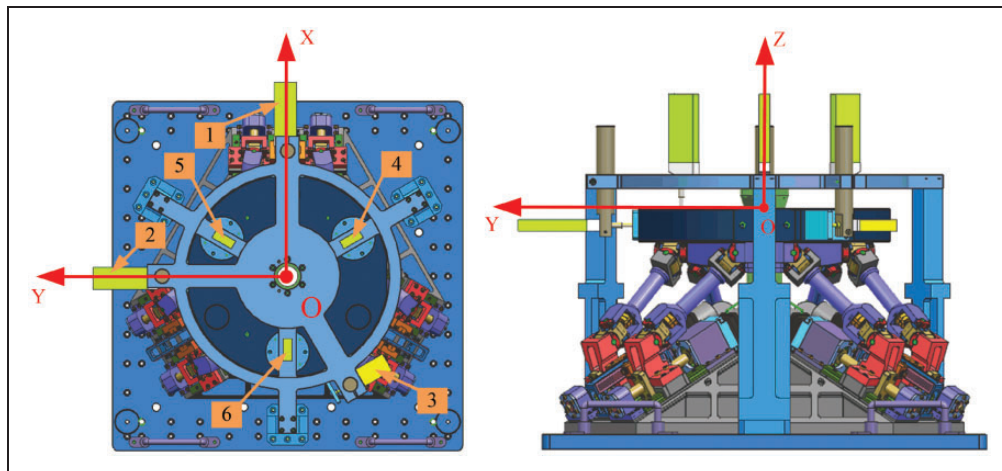


Figure 16. Definition of coordinate system of parallel platform and layout of grating length gauges.

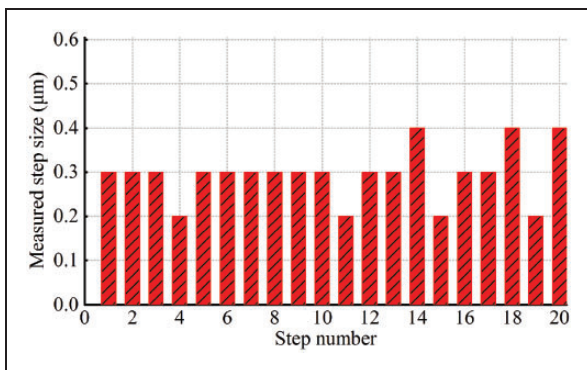
**Table 5.** Grating ruler code values recorded by the reading heads.

Pose	First reading head	Second reading head	Third reading head	Fourth reading head	Fifth reading head	Sixth reading head
Initial position	1337649	1339781	1343800	1354882	1338914	1338056
$P'_1$	1411879	1341340	1286167	1586819	1552783	1334924
$P'_2$	1297453	1400958	1573731	1290017	1173293	1370537
$P'_3$	1121413	1284027	1324886	1287021	1380998	1270520

**Table 6.** Comparison of numerical iterative results and test results.

Slider displacement		$S_1$ (mm)	$S_2$ (mm)	$S_3$ (mm)	$S_4$ (mm)	$S_5$ (mm)	$S_6$ (mm)
$P'_1$	I	3.711476	0.077932	-2.881693	11.596841	10.693436	-0.156632
$P'_1$	T	3.711500	0.077950	-2.881650	11.596850	10.693450	-0.156600
$P'_2$	I	-2.009840	3.058807	11.496529	-3.243284	-8.281066	1.624013
$P'_2$	T	-2.009800	3.058850	11.496550	-3.243250	-8.281050	1.624050
$P'_3$	I	-10.811827	-2.787744	-0.945736	-3.393077	2.104189	-3.376822
$P'_3$	T	-10.811800	-2.787700	-0.945700	-3.393050	2.104200	-3.376800

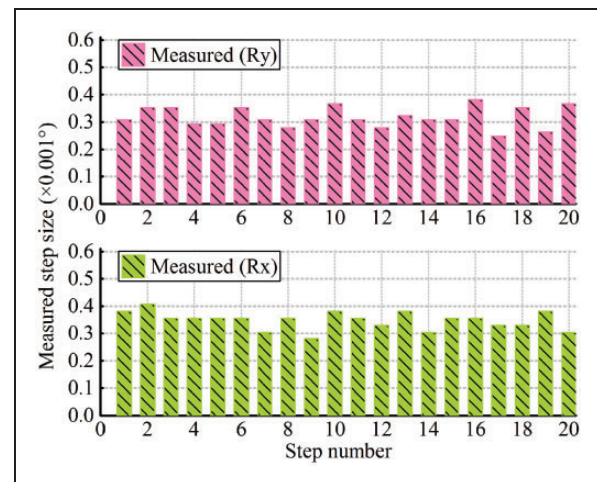
I: Iterative algorithm; T: Test study.

**Figure 17.** Translational resolution along Z-axis.

into the next motion cycle. Repeat the previous step until the position error is smaller than the preset tolerance, so the motor stops moving.

The definition of the coordinate system of the parallel platform and the layout of the grating length gauges are shown in Figure 16. The first and second length gauges are used to test the translational displacements along the X and Y directions, respectively. The third length gauge is used to test the angular displacement  $R_z$ . The fourth, fifth, and sixth length gauges are used to test the translational displacements along the Z direction and the angular displacements  $R_x$  and  $R_y$ , respectively.

Three arbitrary poses  $P'_1$ ,  $P'_2$ , and  $P'_3$  of the simulated load connected to the mobile platform (frame  $O_P - X_P Y_P Z_P$ ) with respect to the base frame  $O_B - X_B Y_B Z_B$  are selected, as given in Table 4. The accuracy of the three poses can be guaranteed by the test system in Figure 15.

**Figure 18.** Rotational resolution around X-axis and Y-axis.

When the mobile platform is controlled from the initial position to poses  $P'_1$ ,  $P'_2$ , and  $P'_3$  separately, the displacements of six sliders are measured by Renishaw reading head fixed on each slider. Before and after the actuating movements of the sliders, the grating code values recorded by the reading heads are shown in Table 5.

According to the changes of the grating code values and resolution of reading head (Renishaw, RL26BAE050D50A series, resolution 50 nm), the displacement of the each slider can be calculated. The numerical iterative results of inverse solution are compared to the test results in Table 6.

Table 6 shows that the results of the numerical iterative calculations are in good agreement with the inverse solution test results and that the differences

between these two sets of results are smaller than 44 nm. These differences are caused mainly by coupling effect of various errors, such as manufacturing errors of parts and components, assembly error of the platform, backlash or friction of the moving parts, the initial position error, pose measurement error and sliders' measurement errors.

### Motion performance test

The motion performance of the parallel platform is also measured using the test devices shown in Figure 15. Because the parallel platform is used as an adjustment mechanism of the third mirror in an optical system, the focusing movement along Z-axis,

yaw motion around the X-axis and the pitch motion around the Y-axis are particularly important, which directly affect the imaging quality of the optical system. So the translation of the mobile platform along the Z-axis, and the rotation about the X-axis and Y-axis are selected to test in this paper. When driving the motors of the lower-joint actuators, the six sliders move along their guides and the displacement of each driving slider is equal to the corresponding result of the inverse kinematics solution.

**Resolution.** In order to evaluate the adjusting capacity of the parallel platform, the translational movements along the Z-axis under  $0.3\mu\text{m}$  commanded step size are measured continuously for 20 steps as shown in

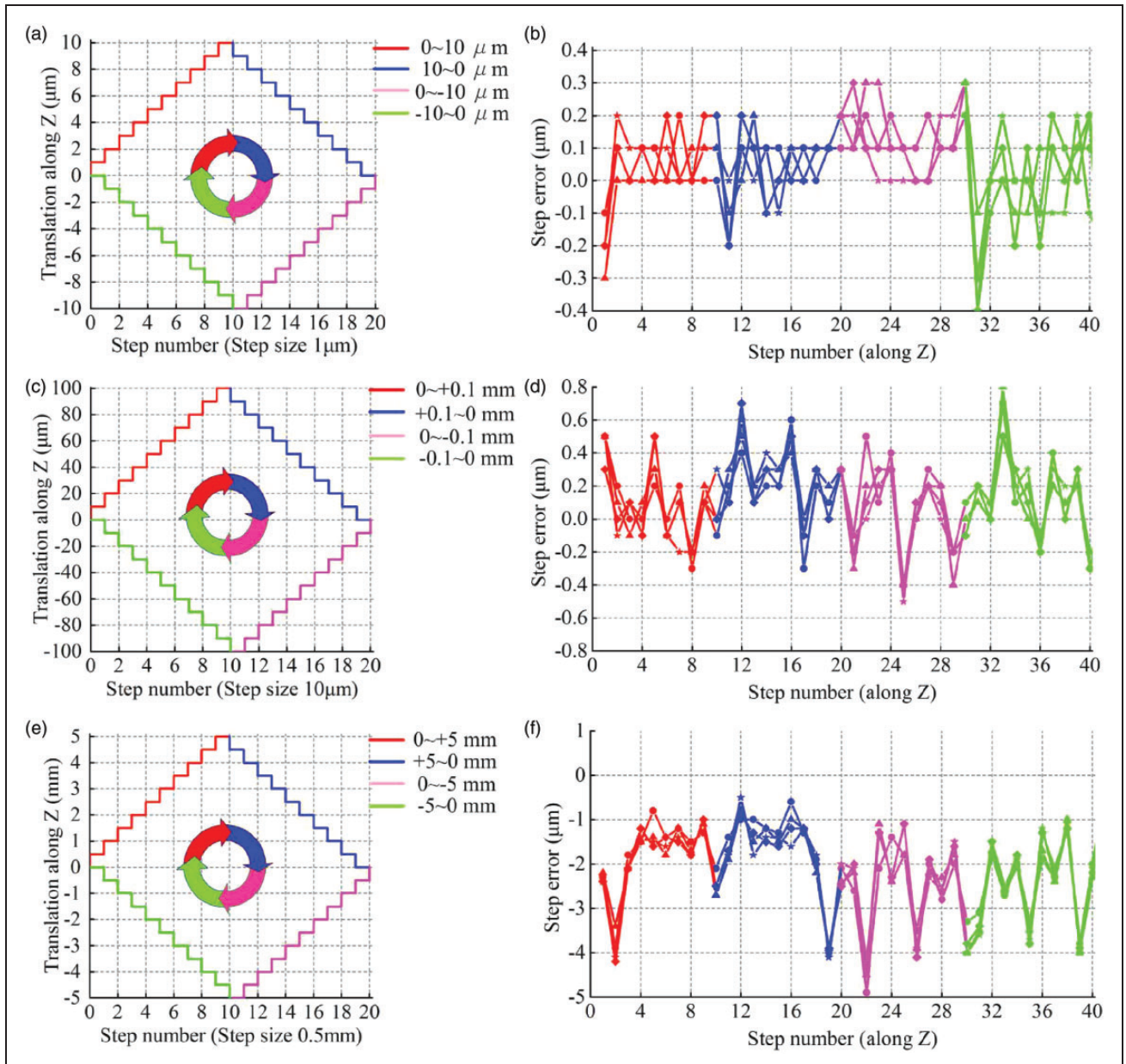


**Figure 19.** Test results of translation of mobile platform along Z-axis.

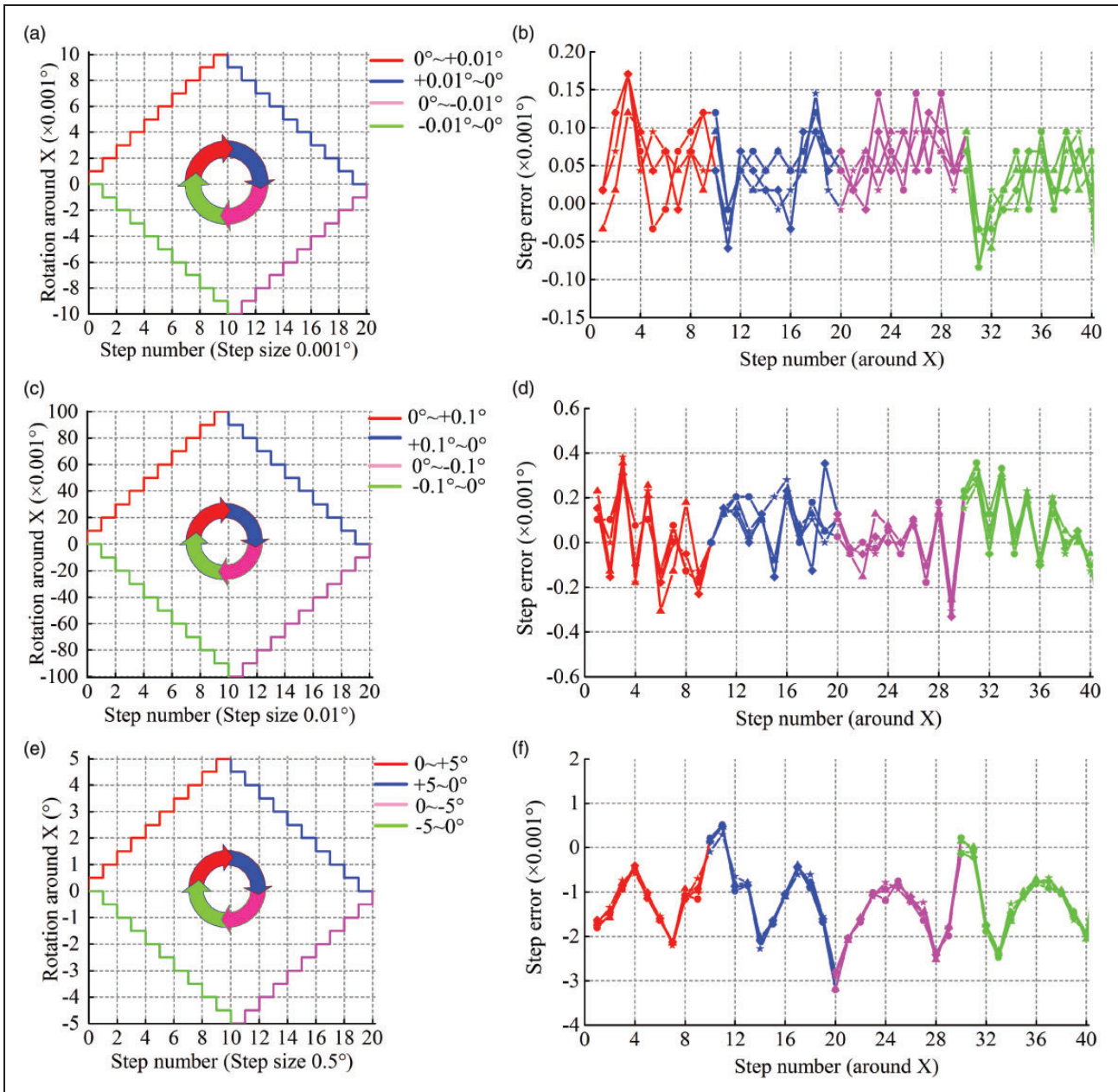


**Figure 20.** Test results of rotation of mobile platform about X-axis.

**Table 7.** Testing results of the rotation around Y-axis.

Test range (°)	Step size (°)	Absolute adjustment precision (°)	Repetitive adjustment precision (°)
-0.01~+0.01	0.001	0.000141	0.000116
-0.1~+0.1	0.01	0.000348	0.000220
-5~+5	0.5	0.004912	0.000984

Figure 17. The measurements of rotation around the X-axis and Y-axis with  $0.0003^\circ$  commanded movements are performed for continuous 20 steps, respectively, as illustrated in Figure 18.

The measurements show that the translational resolution along the Z axis is  $0.295\mu\text{m} \pm 0.060\mu\text{m}$  and the rotational resolutions around the X-axis and Y-axis are  $0.0003486^\circ \pm 0.0000321^\circ$  and  $0.0003181^\circ \pm 0.0000370^\circ$ , respectively. The standard error obeys the principle of one sigma.

**Adjusting accuracy.** The mobile platform is controlled to translate along the Z-axis in the order of  $0 \rightarrow +10\mu\text{m} \rightarrow 0 \rightarrow -10\mu\text{m} \rightarrow 0$  in  $1\mu\text{m}$  steps,  $0 \rightarrow +100\mu\text{m} \rightarrow 0 \rightarrow -100\mu\text{m} \rightarrow 0$  in  $10\mu\text{m}$  steps, and  $0 \rightarrow +5\text{mm} \rightarrow 0 \rightarrow -5\text{mm} \rightarrow 0$  in  $0.5\text{mm}$  steps, where this entire translation is repeated four times. Test results of the translational movement of the mobile platform are shown in Figure 19.

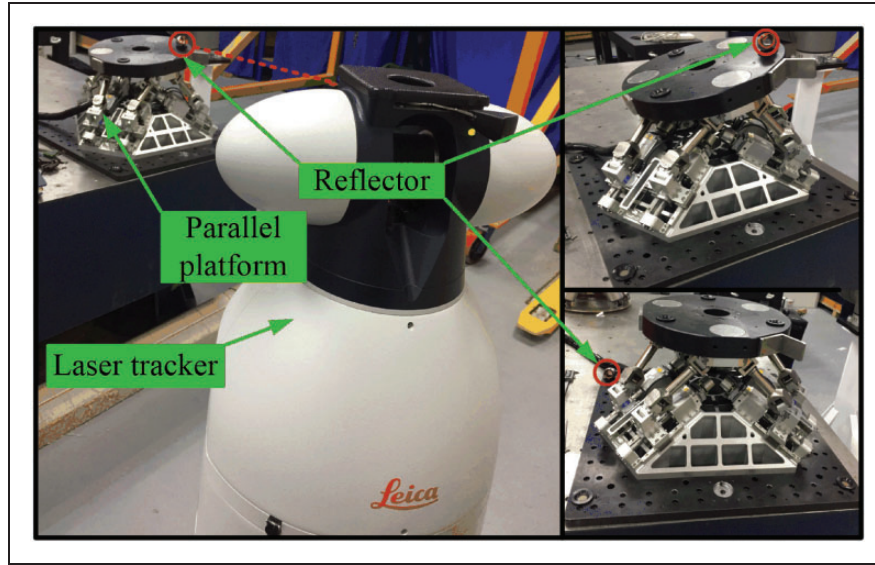


**Figure 21.** Measurement of motion stroke.

By processing the test data in Figure 19, it can be seen that when the mobile platform translates along the Z-axis in  $1\mu\text{m}$  steps,  $10\mu\text{m}$  steps and  $0.5\text{mm}$  steps, the absolute adjusting steps accuracies of the parallel manipulator are  $0.4\mu\text{m}$ ,  $0.8\mu\text{m}$ , and  $4.9\mu\text{m}$ , respectively, and the repetitive adjustment precisions are  $0.3\mu\text{m}$ ,  $0.5\mu\text{m}$ , and  $1.0\mu\text{m}$ , respectively.

Similarly, the mobile platform is controlled to rotate about the X-axis in the order of  $0^\circ \rightarrow +0.01^\circ \rightarrow 0^\circ \rightarrow -0.01^\circ \rightarrow 0^\circ$  in  $0.001^\circ$  steps,  $0^\circ \rightarrow +0.1^\circ \rightarrow 0^\circ \rightarrow -0.1^\circ \rightarrow 0^\circ$  in  $0.01^\circ$  steps, and  $0^\circ \rightarrow +5^\circ \rightarrow 0^\circ \rightarrow -5^\circ \rightarrow 0^\circ$  in  $0.5^\circ$  steps, where this entire rotation sequence is repeated four times. Test results of the rotational movement of the mobile platform are shown in Figure 20.

From the test results in Figure 20, when the mobile platform rotates about the X-axis in  $0.001^\circ$  steps,  $0.01^\circ$  steps and  $0.5^\circ$  steps, the absolute adjusting steps accuracies of the parallel manipulator are found to be  $0.000171^\circ$ ,  $0.000382^\circ$ , and  $0.003206^\circ$ , respectively, and the repetitive adjustment precisions are found to be  $0.000127^\circ$ ,  $0.000356^\circ$ , and  $0.000455^\circ$ , respectively.

Rotation of the mobile platform about the Y-axis is also measured in a way that is the same with Rx motion test, and the results are shown in the Table 7.

The main causes of movement error of the platform include the following: 1) manufacturing errors of parts and components; 2) assembly error of the platform; 3) backlash or friction of the moving parts; 4) the definition of the initial position of the upper platform being different from the theoretical zero position; and 5) measurement errors introduced by the testing process.

**Motion stroke.** When the moving ranges of the parallel platform become larger, measuring range of the grating length gauge is no longer satisfied with the test requirements, and the measurement error of the test

**Table 8.** Results of the motion stroke test.

X (mm)	Y (mm)	Z (mm)	Rx ( $^\circ$ )	Ry ( $^\circ$ )	Rz ( $^\circ$ )
$\pm 35$	$\pm 33$	$\pm 34$	$\pm 13$	$\pm 13$	$\pm 15$

system (shown in Figure 15) also increases gradually. So laser tracker (Leica, tracking accuracy  $0.01\text{mm}$ ) is utilized to measure the motion strokes of the parallel platform in six directions. Laser tracker reflectors are placed into the circular grooves which are processed on the bottom platform and simulated load, respectively, as shown in Figure 21.

Translational distances along X, Y and Z axes, and rotational ranges around X, Y and Z axes of the parallel platform are displayed in Table 8.

## Conclusions

This paper presented the inverse kinematics of a novel 6-DOF parallel platform with 6-P-RR-R-RR kinematic chains. The platform is characterized by offset RR-joints. Owing to the existence of the offset-joint variables, the inverse kinematics problem of the platform is much more complicated than that of a parallel platform with conventional configurations, such as 6-UCU, 6-SPS, 6-UPS, and 6-UPU. In this work, the characteristics of the offset RR-joints were studied and the kinematic constraint equations of these joints were provided. Then, a highly nonlinear equation set containing 18 equations as well as 18 variables for the inverse kinematics problem of the 6-DOF parallel platform was derived and a numerical iterative method was used to solve the kinematics problem. Furthermore, the accuracy of the inverse solution was verified by numerical co-simulations using ADAMS and MATLAB. Finally, the initial position of the platform was determined by a precision measuring arm. A test system was

constructed, and then inverse kinematics solution, resolutions and adjusting steps accuracies of the platform were tested using the system. Motion strokes of the parallel mechanism were measured by a laser tracker.


### Declaration of Conflicting Interests

The author(s) declared no potential conflicts of interest with respect to the research, authorship, and/or publication of this article.

### Funding

The author(s) disclosed receipt of the following financial support for the research, authorship, and/or publication of this article: This work was supported by the National Natural Science Foundation of China (grant number 11672290); the Jilin Scientific and Technological Development Program (grant number 20160520074JH); and the Youth Innovation Promotion Association, Chinese Academy of Sciences (grant number 2014195).

### ORCID iD

Ha-si-ao-qi-er Han  <http://orcid.org/0000-0002-8427-3377>

### References

- Gough VE. Contribution to discussion of papers on research in automobile stability. *Proc Automotive Division Inst Mech Eng* 1956; 171: 392–395.
- Stewart D. A platform with six degrees of freedom. *Proc Inst Mech Eng* 1965; 180: 371–386.
- Hunt KH and Primrose EJJ. Assembly configurations of some in-parallel-actuated manipulators. *Mech Mach Theory* 1993; 28: 31–42.
- Shiga Y, Tanaka Y, Goto H, et al. Design of six degree-of-freedom tripod parallel mechanism for flight simulator. *Int J Auto Technol* 2011; 5: 715–721.
- Wu DS, Gu HB and Li P. Comparative study on dynamic identification of parallel motion platform for a novel flight simulator. In: *IEEE international conference on robotics and biomimetics*, Guilin, China, 19–23 December 2009, pp.2232–2237.
- Zhang JZ, Yu HN, Gao F, et al. Application of a novel 6-DOF parallel robot with redundant actuation for earthquake simulation. In: *IEEE international conference on robotics and biomimetics (ROBIO)*, Tianjin, China, 14–18 December 2010, pp.513–518.
- Yang JF, Xu ZB, Wu QW, et al. Dynamic modeling and control of a 6-DOF micro-vibration simulator. *Mech Mach Theory* 2016; 104: 350–369.
- Yang JF, Xu ZB, Wu QW, et al. Design of six dimensional vibration isolation system for space optical payload. *Opt Precision Eng* 2015; 23: 1347–1357.
- Wu J, Chen XL and Wang LP. Design and dynamics of a novel solar tracker with parallel mechanism. *IEEE/ASME Transact Mech* 2016; 21: 88–97.
- Wu J, Zhang BB and Wang LP. Optimum design and performance comparison of a redundantly actuated solar tracker and its nonredundant counterpart. *Solar Energy* 2016; 127: 36–47.
- Cleary K and Brooks T. Kinematic analysis of a novel 6-DOF parallel manipulator. In: *Proceedings of the IEEE international conference on robotics and automation*, Atlanta, GA, 2–6 May 1993, pp.708–713.
- Oba Y, Yamada Y, Igarashi K, et al. Replication of skilled polishing technique with serial-parallel mechanism polishing machine. *Precis Eng* 2016; 45: 292–300.
- Kerr DR. Analysis, properties, and design of a Stewart-platform transducer. *J Mech Transmission Automat Des* 1989; 111: 25–28.
- Merlet JP. *Parallel robots*. 2nd ed. Netherlands: Springer, 2006.
- Tian Y, Shirinzadeh B and Zhang D. A flexure-based mechanism and control methodology for ultra-precision turning operation. *Precis Eng* 2009; 33: 160–166.
- Yao Q, Dong JY, Ferreira PM, et al. A novel parallel-kinematics mechanisms for integrated, multi-axis nano-positioning: Part I. *Precis Eng* 2008; 32: 7–19.
- Teo TJ, Chen IM and Yang GL. A large deflection and high payload flexure-based parallel manipulator for UV nanoimprint lithography: Part II. Stiffness modeling and performance evaluation. *Precis Eng* 2014; 38: 872–884.
- Li YM and Xu QS. Design and analysis of a totally decoupled flexure-based xy parallel micromanipulator. *IEEE Trans Robot* 2009; 25: 645–657.
- Liaw HC and Shirinzadeh B. Robust generalized impedance control of piezo-actuated flexure-based four-bar mechanisms for micro/nano manipulation. *Sens Actuat A Phys* 2008; 148: 443–453.
- Liaw HC, Shirinzadeh B and Smith J. Robust motion tracking control of piezo-driven flexure-based four-bar mechanism for micro/nano manipulation. *Mechatronics* 2008; 18: 111–120.
- Brouwer DM, De Jong BR and Soemers HMJR. Design and modeling of a six DOFs MEMS-based precision manipulator. *Precis Eng* 2010; 34: 307–319.
- Dalvand MM, Shirinzadeh, et al. Motion control analysis of parallel robot assisted minimally invasive surgery/microsurgery system (PRAMiSS). *Robot CIM-Int Manuf* 2013; 29: 318–327.
- Zimmermann M, Krishnan R, Raabe A, et al. Robot-assisted navigated endoscopic ventriculostomy: implementation of a new technology and first clinical results. *Acta Neurochir* 2004; 146: 697–704.
- Li T and Payandeh S. Design of spherical parallel mechanisms for application to laparoscopic surgery. *Robotica* 2002; 20: 133–138.
- Shoham M, Burman M, Zehavi E, et al. Bone-mounted miniature robot for surgical procedures: concept and clinical applications. *IEEE Trans Robot Automat* 2003; 19: 893–901.
- Brandt G, Zimolong A, Carrat L, et al. CRIGOS: a compact robot for image-guided orthopedic surgery. *IEEE Trans Inf Technol Biomed* 1999; 3: 252–260.
- Nakano T, Sugita N, Ueta T, et al. A parallel robot to assist vitreoretinal surgery. *Int J CARS* 2009; 4: 517–526.
- Neill DR, Sneed R, Dawson J, et al. Baseline design and requirements for the LSST hexapod and rotator. *Adv Optical Mech Technol Telescopes Instrument* 2014; 9151: 91512B1–91512B16.
- Ford V, Cartera C, Delrezb C, et al. Jitter studies for the secondary and tertiary mirror systems on the thirty meter telescope. *Adv Optical Mech Technol Telescopes Instrument* 2014; 9151: 91512H1–91512H15.
- Nieto D, Griffiths S, Humensky B, et al. Construction of a medium-sized Schwarzschild-

- Couder telescope as a candidate for the Cherenkov Telescope Array development of the optical alignment system. *Physics*; In: The 34th International Cosmic Ray Conference, The Hague, The Netherlands, 30 July–6 August, 2015 The Hague, The Netherlands; pp. 1–8.
31. Dalvand MM and Shirinzadeh B. Kinematics analysis of 6-DOF parallel micro-manipulators with offset U-joints. *Int J Intell Mechatronics Rob* 2012; 2: 28–40.
  32. Dalvand MM, Shirinzadeh B and Nahavandi S. Inverse kinematics analysis of 6-RRCRR parallel manipulators. In: *ASME international conference on advanced intelligent mechatronics (AIM)*, Wollongong, Australia, 9–12 July 2013, pp.644–648.
  33. Staicu S, Ocnareescu C and Ungureanu LM. Inverse kinematics of a parallel flight simulator. *UPB Scientific Bulletin* 2014; 76: 3–12.
  34. Wang D and Fan R. Design and nonlinear analysis of a 6-DOF compliant parallel manipulator with spatial beam flexure hinges. *Precis Eng* 2016; 45: 365–373.
  35. Gan D, Liao Q, Dai JS, et al. Forward displacement analysis of a new 1CCC–5SPS parallel mechanism using Gröbner theory. *Proc Inst Mech Eng C* 2009; 223: 1233–1241.
  36. Fu JX, Gao F, Pan Y, et al. Forward kinematics solutions of a special six-degree-of-freedom parallel manipulator with three limbs. *Adv Mech Eng* 2015; 7: 1–11.
  37. Huang X, Liao Q and Wei S. Closed-form forward kinematics for a symmetrical 6-6 Stewart platform using algebraic elimination. *Mech Mach Theory* 2010; 45: 327–334.
  38. Xu G and Yang SM. Universal workspace characteristics of Gough-Stewart platform and its analytic solution. *Opt Precision Eng* 2008; 16: 257–264.
  39. Han CY, Xu ZB, Wu QW, et al. Optimization design and error distribution for secondary mirror adjusting mechanism of large optical payload. *Opt Precision Eng* 2016; 24: 1094–1103.
  40. Song YM, Zhang JT, Lian BB, et al. Kinematic calibration of a 5-DOF parallel kinematic machine. *Precis Eng* 2016; 45: 242–261.
  41. Shi HL, Su HJ, Dagalakos N, et al. Kinematic modeling and calibration of a flexure based hexapod nanopositioner. *Precis Eng* 2013; 37: 117–128.
  42. Ji CY, Chen TC and Lee YL. Investigation of kinematic analysis and applications for a 3-RRPS parallel manipulator. *J Chinese Soc Mech Eng* 2007; 28: 623–632.
  43. Takeda Y, Xiao X, Hirose K, et al. Kinematic analysis and design of 3-RPSR parallel mechanism with triple revolute joints on the base. *Int J Automat Technol* 2010; 4: 346–354.
  44. Singh Y, Vinoth V and Santhakumar M. Inverse kinematic solution of a 6-DOF (3-RPRS) parallel spatial manipulator. In: *The 3rd joint international conference on multibody system dynamics, the 7th Asian conference on multibody dynamics*, BEXCO, Busan, Korea, 30 June–3 July 2014.
  45. Ryu JH, Song J and Kwon DS. A nonlinear friction compensation method using adaptive control and its practical application to an in-parallel actuated 6-DOF manipulator. *Control Eng Practice* 2001; 9: 159–167.
  46. Tsai KY and Lee TK. 6-DOF isotropic parallel manipulators with three PPSR or PRPS chains. In: *12th IFTOMM World Congress*, Besançon, France, 18–21 June 2007.
  47. Kim WK, Yong KB and Cho HS. Closed-form forward-position solution for a 6 DoF 3-PPSP parallel mechanism and its implementation. *Int J Robotics Res* 2001; 20: 85–99.
  48. Liu MS, Cao Y, Zhang QJ, et al. Kinematics and workspace analyses of 3/3-RRRS parallel manipulator. *Appl Mech Mater* 2012; 155–156: 1090–1095.
  49. Liu Y, Wu H, Yang Y, et al. Symmetrical workspace of 6-UPS parallel robot using tilt and torsion angles. *Math Probl Eng* 2018; 2018: 1–10.
  50. Ruizgarcia J, Chaparroaltamirano D, Zavalayoe R, et al. Direct and inverse dynamics modeling of a 6-PUS parallel robot. In: *IEEE international conference on mechatronics, electronics and automotive engineering (ICMEAE)*, Morelos, Mexico, 19–22 November 2013.
  51. Joumah AA and Albitar C. Design optimization of 6-RUS parallel manipulator using hybrid algorithm. *I. J. Inform Technol Comput Sci* 2018; 10: 83–95.
  52. Mirshekari E, Ghanbarzadeh A, Shirazia KH, et al. Structure comparison and optimal design of 6-RUS parallel manipulator based on kinematic and dynamic performances. *Lat Am J Solids Stru* 2016; 13: 2414–2438.
  53. Liu GJ, Zheng ST, Ogbope PO, et al. Inverse kinematic and dynamic analyses of the 6-UCU parallel manipulator. *Appl Mech Mater* 2012; 127: 172–180.
  54. Yu Y, Xu ZB, Wu QW, et al. Kinematic analysis and testing of a 6-RRRPRR parallel manipulator. *Proc IMechE, Part C: J Mechanical Engineering Science* 2016; 231: 2515–2527.
  55. Han CS, Hudgens JC, Tesar D, et al. Modeling, synthesis, analysis and design of high resolution micromanipulator to enhance robot accuracy. In: *IEEE RSG International workshop on intelligent robots and systems IROS '91. 'intelligence for mechanical systems*, Osaka, Japan, 3–5 November 1991.
  56. Tsai LW and Tahmasebi F. Synthesis and analysis of a new class of six-degree-of-freedom parallel minimanipulators. *J Robot Syst* 1993; 10: 561–580.
  57. Wang S, Hikita H, Hanajima N, et al. Kinematics and force analysis of a 6 D.O.F. parallel mechanism with elastic joints. In: Jadran Lenarčič, Manfred L. Husty (eds.), *Advances in robot kinematics: analysis and control*. Springer: Netherlands, 1998, pp.87–96.
  58. Ji P and Wu HT. Kinematics analysis of an offset 3-UPU translational parallel robotic manipulator. *Rob Auton Syst* 2003; 42: 117–123.
  59. Hu B and Lu Y. Analyses of kinematics, statics, and workspace of a 3-RRPRR parallel manipulator and its three isomeric mechanisms. *Proc IMechE, Part C: J Mechanical Engineering Science* 2008; 222: 1829–1837.
  60. Wang J and Masory O. On the accuracy of a Stewart platform. I. The effect of manufacturing tolerances. In: *IEEE international conference on robotics and automation*, Atlanta, GA, 2–6 May 1993, pp.114–120.
  61. Daney D. Kinematic calibration of the Gough platform. *Robotica* 2003; 21: 677–690.
  62. Großmann K and Kauschinger B. Eccentric universal joints for parallel kinematic machine tools: variants and kinematic transformations. *Prod Eng Res Devel* 2012; 6: 521–529.
  63. Gloess R and Lula B. Challenges of extreme load hexapod design and modularization for large ground-based telescopes. *Proc SPIE Int Soc Opt Eng* 2010; 7739: 327–330.